A Highly Efficient Spherical Luneburg Lens for Low Microwave Frequencies Realized with a Metal-based Artificial Medium

Maral Ansari, *Student Member, IEEE*, Bevan Jones, *Life Member, IEEE*, He Zhu, Negin Shariati, and Y. Jay Guo, *Fellow, IEEE*

***Abstract*—This paper describes a novel spherical lens antenna constructed of planar layers of light-weight foam with equally spaced conducting inclusions of varying sizes on an orthogonal grid. This construction largely overcomes the problems of weight and cost that have tended to make larger low frequency Luneburg lenses impractical. A penalty for this type of design is that some anisotropy exists in the lens's dielectric. This effect is examined using both ray tracing techniques and full-wave simulation and it is found that the principal consequence is that the focal length of the lens varies in different directions. Methods for mitigating the effect are proposed. A prototype lens antenna intended for cellular use in the band 3.3 – 3.8 GHz with dual linear slant polarized feeds was designed and constructed to confirm the findings. Measured results show a peak gain of 23 dBi which is less than 1 dB lower than the maximum possible directivity from the lens's cross section area. Scanning loss is less than 0.8 dB over the whole sphere. Simulated and measured performance show excellent agreement over the whole sphere. The overall performance of the prototype lens antenna demonstrates that this type of lens should be very suitable for use in high-gain multibeam antennas at lower microwave frequencies.**

***Index Terms*—Anisotropy, conducting inclusions, dual linear slant polarized, light-weight, ray-tracing, spherical Luneburg lens**

I. Introduction

The spherical Luneburg lens has a number of features that make it uniquely suitable for realizing multibeam antennas. Owing to its spherical symmetry, the beam shape in principle does not vary with scan angle [1]. To form a narrow beam in two dimensions, there is no need to employ a large number of radiating elements as the aperture forming the beam is the lens itself. No additional feed network is needed to radiate dual-polarization as the lens propagates orthogonal polarizations provided the dielectric is reasonably isotropic. The lens can be configured with a refractive index profile that is 1 at the outer surface, thus making the reflection low. As the lens design is based on geometrical optics, it is inherently a wide-band structure, limited principally by the artificial dielectric.

Alternative designs for multibeam antennas employ beam-forming networks such as one-dimensional (1D) or two dimensional (2D) Butler matrices [2]–[9], typically requiring duplication of hardware to achieve dual-polarization. These circuits easily result in a few dBs of loss, and the array pattern performance tends to be worse than that of the Luneburg lenses.

Spherical Luneburg lenses would therefore appear to be among the most attractive multibeam antennas for wireless communications. Despite the advantages, such designs have not found wide application in current cellular networks except for specialized applications such as providing multicell coverage to handle extreme traffic density as in sports stadiums or for portable base stations at for example, outdoor concert events [10]. There is also a niche application for fixed rural stations where beams can be steered to villages and small communities for fixed wireless service. Reasons for the lack of acceptance include high weight and poor public acceptance of the spherical shape. It is expected that in the future such lenses will provide a cheap alternative to massive multiple-input-multiple-output (MIMO) antennas in fifth-generation (5G) systems. Compared with array antennas, Luneburg lenses can be flexible, efficient, and low-cost [11], [12].

Much of the recent work on Luneburg lenses has been directed at cylindrical structures at higher frequencies. Parallel-plate Luneburg lenses with directive beams in their H-plane are described in [13]–[16]. A design with high directivity in the E-plane is described in [17]. However, when it comes to lower microwave frequencies, most modern communications systems require dual-polarization and high directivity in both planes. It is in this situation that the economy and simplicity of the spherical Luneburg lenses come to the fore.

Spherical Luneburg lens antennas of flat shape have been developed using transformation optics [18], [19]. Wide scanning angles and dual-polarization have been realized in [19]. Such structures offer highly directive antennas with low profile. Novel spherical Luneburg lenses constructed using different techniques have been reported [20]–[22]. In [23] a lens antenna is designed using 3D printing technology. This design has high directivity in both planes, and is reasonably efficient. The measured gain degradation is mainly attributed to the dielectric loss of the 3D printing material. The effect on polarization of the rather extreme anisotropy produced in a spherical Luneburg lens constructed of parallel, tapered layers of pure dielectric has been examined in [22]. However, the effect on other parameters such as focal length was not considered.

The technique of using periodically located holes drilled in dielectric slabs has been reported [24]–[26]. These methods

Manuscript submitted June 14, 2020; revised September 6, 2020; Accepted November 22, 2020. (Corresponding author: Maral Ansari.)

The authors are with the Global Big Data Technologies Centre (GBDTC), University of Technology Sydney, Ultimo 2007, NSW, Australia (email: Maral.ansari@student.uts.edu.au)

This article has been accepted for publication in a future issue of this journal, but has not been fully edited. Content may change prior to final publication. Citation information: DOI 10.1109/TAP.2020.3044638, IEEE Transactions on Antennas and Propagation

while suited for high frequencies, are not well suited to designs at lower microwave frequencies as the solid dielectric material is heavy and costly. A series of very innovative sub-6 GHz Luneburg lenses has found some application in the communications industry. These lenses use a graded index material comprising randomly oriented sub-resonant wires encased in foam [27]. This work largely overcomes weight problems, but is still costly and the design is not fully deterministic. The design described in this work shows that very low loss is possible if the lens is made using an artificial dielectric material comprising a low-density foam with conducting inclusions. Such construction results in a low-weight, low-cost structure. Weight has been a significant problem with earlier designs using solid dielectric materials. This situation is further improved if the conducting inclusions are made from lightweight plastic with a copper or silver coating and these are supported in low-density foam.

This paper presents a novel and practical Luneburg lens design applicable for use in the frequency range of 0.5 to 12 GHz. The lens is constructed of equal thickness, planar layers of extruded polystyrene foam (XPS) with embedded spherical or cubic shaped conducting inclusions set into each layer on a uniform cubic grid. The layers which are circular in shape are stacked to form the spherical shape of the lens. The sizes of the inclusions but not their spacings are varied to control the local velocity of propagation or refractive index. Equal spacing of the inclusions on an orthogonal grid provides a major advantage from a construction viewpoint as it permits the use of parallel equal thickness layers. A negative consequence of this geometry is that there is some anisotropy in refractive index as a function of inclination of propagation direction to the grid of inclusions. Using ray tracing based on the refractive index profile, the lens is designed to position the focus at a convenient location beyond the body of the lens.

Using full-wave calculation of the effective refractive index of arrays of equal sized inclusions and ray tracing analysis of the effect on focusing of the variations that occur with incidence angle, it is shown that the principal effect of the anisotropy is to cause the focal length of the lens to vary and hence the required position of the feed. If the effect is not corrected, it leads to gain reduction and degradation of cross-polar ratio if orthogonal polarizations are present.

A prototype lens antenna was designed and constructed according to these concepts for cellular use in the current time-division-duplex (TDD) band of 3.3 to 3.8 GHz to demonstrate the effectiveness of the method. The diameter of the lens is 400 mm (4.5λ) at mid-band providing a half-power beamwidth of 14° and a gain of 23 dBi. It is fed by a square-waveguide feed providing dual linear 45° slant polarization as required for cellular antennas.

The analysis, design and test results are described in the rest of the paper as follows. Section II describes the design of the artificial dielectric, the optical ray tracing technique used to design the lens antenna and the analysis of the source and effects of the anisotropy on performance. Section III describes the detailed design of the feed and lens components. Fabrication and measurement results of the prototype lens antenna are discussed in section IV. Section V contains an assessment of the success of techniques described.

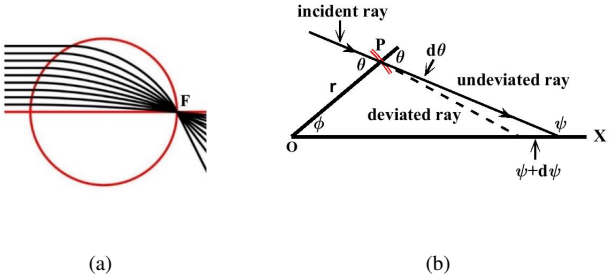

(a) (b)

Fig. 1. (a) Ray trace of original Luneburg lens with focus (F). (b) Ray bending at arbitrary point P. (Constant refractive index contour indicated in red)

II. Optical Analysis and Design of the Lens

In this section, the design and analysis of the Luneburg lens is described. The required refractive index profile is obtained by geometrical optics. The focus is located by optical ray tracing through the lens. The rays in an incident parallel beam are traced through the lens with a given dielectric profile and the distances of the exiting rays from a desired focus are minimized by adjusting the refractive index profile. After the optimum profile has been determined, the refractive index of uniform arrays of metal inclusions is analyzed using HFSS. The refractive index as a function of the size of the inclusions for a fixed chosen spacing is found, and the results are used to determine the sizes of all the inclusions within the lens.

A. Ray Tracing and Position of Focus

The original Luneburg lens is a dielectric sphere whose index of refraction follows the equation:

$$n(r) = \sqrt{2 - r^2} \tag{1}$$

where r is the radius normalized so that the surface of the lens is at $r = 1$. For this profile of refractive index, the focal point occurs at the surface of the lens and the rays within the lens follow elliptical paths as shown in Fig. 1(a). However, in practice it is more convenient to locate the focus outside the lens, particularly if an open waveguide is used as the feed antenna as the phase center of such a feed lies within the waveguide behind its aperture.

In order to change the focal length, the refractive index profile in the lens must change. For this purpose, ray paths through the lens with a prescribed refractive index profile are calculated by solving a differential equation. From a bunch of parallel rays on the left-hand side of the lens in Fig. 1(a) the paths to where they exit on the right-hand side of the lens are calculated. After exiting the lens, the ray paths become straight again. At this point, the minimum distance of each ray from a desired focal point is obtained. Finally, the refractive index profile of the lens is optimized to minimize the mean square errors. The differential equation can be obtained as follows.

This article has been accepted for publication in a future issue of this journal, but has not been fully edited. Content may change prior to final publication. Citation information: DOI 10.1109/TAP.2020.3044638, IEEE Transactions on Antennas and Propagation

TABLE I
COEFFICIENT VALUES DEFINING REFRACTIVE INDEX PROFILES.

Focus Location	a_1	a_2	a_3
R (lens surface)	1.0160	-0.0327	0.0068
1.15R	0.8121	-0.0335	0.0078
1.30R	0.6782	-0.0345	0.0097

⋆ **R=radius of lens (R=200 mm)**.

As shown in Fig. 1(b) an arbitrary ray inclined at an angle ψ to the x-axis passes through a point P(x,y). At P:

$$\frac{dy}{dx} = \tan\psi \tag{2}$$

In the case shown $\frac{dy}{dx}$ and $\tan\psi$ are negative. If the radius vector **r** from the center of the lens to P(x,y) makes an angle ϕ with the x-axis, then the angle of incidence of the ray with the surface of constant refractive index is the angle θ between the ray and **r**. From the diagram in Fig. 1(b).

$$\pi - \theta + \phi = \psi \tag{3}$$

With bending of the ray by $d\theta$, there is a change in ψ of $d\psi = -d\theta$ since at P(x,y), ϕ does not change. The differential form of Snell's law that applies at P is:

$$d\theta = -\tan\theta \frac{dn}{n} \tag{4}$$

where n is the local refractive index. Applying (3) this becomes:

$$d\psi = \tan(\phi - \psi).\frac{dn}{n} \tag{5}$$

$$\frac{d\psi}{dx} = \tan(\phi - \psi).\frac{1}{n}\frac{dn}{dr}.\frac{dr}{dx} \tag{6}$$

Differentiating (2) with respect to x results in (7).

$$\frac{d^2y}{dx^2} = \sec^2\psi.\frac{d\psi}{dx} \tag{7}$$

Substituting (6) in (7):

$$\frac{d^2y}{dx^2} = \sec^2\psi.\tan(\phi - \psi).\frac{1}{n}\frac{dn}{dr}.\frac{dr}{dx} \tag{8}$$

This is the required differential equation for calculating the ray trajectories. To solve the differential equation numerically the right hand side of (8) should be expressed as a function of x, y, $\frac{dy}{dx}$. Each of the terms in this equation can be written as a function of x, y, $\frac{dy}{dx}$:

$$\sec^2\psi = 1 + (\frac{dy}{dx})^2;\ \tan\phi = \frac{y}{x};\ \tan\psi = \frac{dy}{dx}$$

$\frac{1}{n}\frac{dn}{dr}$ is known from the refractive index profile and $\frac{dr}{dx}$ is obtained from $r^2 = x^2 + y^2$. Using (8) along with initial conditions of a point on the ray and slope at that point i.e. x_0, y_0, and $\frac{dy}{dx})_0$ the ray trajectory can be calculated.

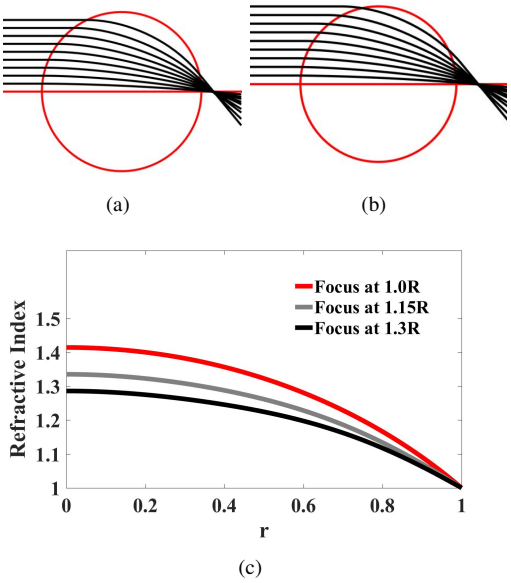

Fig. 2. Ray trace of Luneburg lens when focus is moved outside lens by (a) 0.15R and (b) 0.3R. (c) Corresponding calculated refractive index profiles.

In order to calculate the rays shown in Fig. 1(a) the MATLAB function 'ode45' is used. To determine this figure, the refractive index profile was initially set to $n(r) = \sqrt{2 - r^2}$, which has $n = 1$ at $r = 1$ the surface of the lens and $n = \sqrt{2}$ at the center of the lens. This is the standard Luneburg lens and has the focus at surface of the lens. To move the focus outside the lens the outer boundary of the lens should still have $n = 1$, but the center of the lens has $n < \sqrt{2}$. The refractive index profile is represented by the sum of functions capable of representing curves of this type, each with weighting coefficients that can be selected to adjust the shape as:

$$n(r)^2 = 1 + \sum_{i=1}^{N} a_i \cos\frac{\pi}{2}(2i-1)r \tag{9}$$

The optimization was carried out using the Matlab function 'fminsearch' which uses the Nelder-Mead simplex algorithm. It is found that 3 unknown coefficients are adequate to provide refractive index values accurate to 3 decimal places. N=3 gives satisfactory results.

After the rays leave the lens, they are straight lines. The sum of the squares of the distances of all the rays from the desired focus is calculated and the coefficients a_i are optimized to minimize this quantity. After this process, the rays pass through the desired focus with sufficient accuracy. The corresponding ray plots and the calculated refractive index profiles are shown in Fig. 2. The values of the coefficients found for the three cases shown in Fig. 2(c) are listed in Table I. The $1.15R$ focus position was used for the design of the prototype lens.

This article has been accepted for publication in a future issue of this journal, but has not been fully edited. Content may change prior to final publication. Citation information: DOI 10.1109/TAP.2020.3044638, IEEE Transactions on Antennas and Propagation

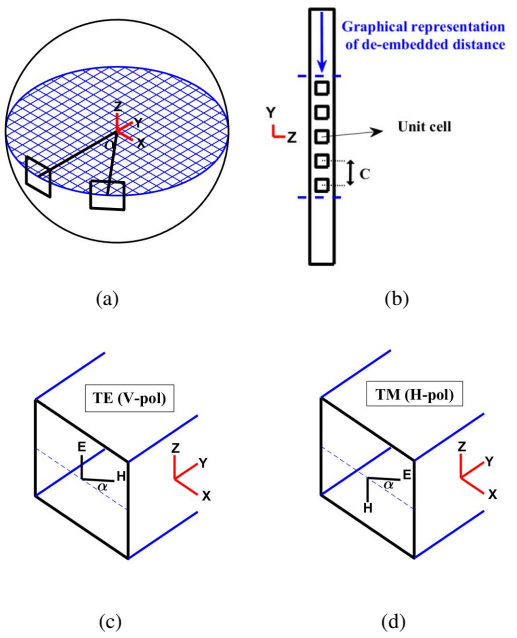

Fig. 3. Calculation of velocity factors with uniform arrays of inclusions. (a) Geometry of lens showing inclination α of feed to array of inclusions. (b) Configuration analyzed. Arrays of inclusions replaced by periodic boundary conditions (PBC). (c),(d) Field directions for TE and TM (relative to y-direction) excitations.

B. Artificial Dielectric and Lens Geometry

The graded refractive index used in the Luneburg lens design is realized by varying the sizes of the periodic inclusions. The gradient-index (GRIN) material consists of parallel layers of foam with conducting spherical [28] or cubic inclusions located on a square grid on the central plane of each layer. In the overall design of the lens antenna, the diameter of the lens is determined by the required beamwidth at low frequencies, and the maximum permissible spacing of the inclusions is determined by the required performance at high frequencies. The thickness of the layers is equal to the spacing of the inclusions so this determines the number of layers. The layers are circular in shape and are stacked vertically in the z-direction to form the spherical shape of the lens.

The inclusions are placed so that their centers are midway between the upper and lower surfaces of the foam sheet. The inclusions then lie on a 3D grid with equal spacing C in the x, y and z-directions. The spacing should be as large as possible to economize construction, but small enough that the resulting medium behaves approximately as a homogeneous medium allowing application of effective medium theory for extraction of refractive index [29]. In this design, the spacing has been chosen as $C = 20$ mm, which is $\lambda/5$ at 3.5 GHz. Since the layer thickness is equal to the spacing of the inclusions, 20 layers are needed to make up the 400 mm diameter of the lens.

Figure. 3 shows the configuration used for calculation of velocity factors of medium with uniform arrays of inclusions. To select the required sizes of the conducting inclusions, an infinite 3D array of equally spaced identical inclusions of a certain size is analyzed. The input wave is launched in free

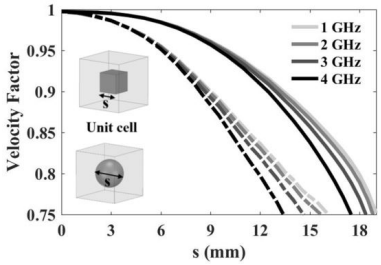

Fig. 4. Velocity factors as a function of inclusion size 's' for spherical inclusions (solid lines) and cubic inclusions (dashed lines) for normal incidence. (cell size C = 20 mm)

space toward the unit cell with E-field in the z-direction (TE) or x-direction (TM). Master and slave boundary conditions are set up around the cell so as to take account of the infinite arrays in the x and z-directions. A group of cells in the y-direction is analyzed and S-parameters relating the input to the first of these cells and the output from the last cell are calculated. The number of cells in the y-direction was chosen to allow for interaction of the fields surrounding the different inclusions through higher modes in the propagation direction. Experimenting with different numbers of cells showed that 5 cells are sufficient.

The velocity factor of the material is extracted from the S-parameters as shown below:

$$\begin{bmatrix} b_1 \\ b_2 \end{bmatrix} = S \begin{bmatrix} a_1 \\ a_2 \end{bmatrix} \tag{10}$$

The T-matrix is determined by:

$$\begin{bmatrix} a_1 \\ b_1 \end{bmatrix} = T \begin{bmatrix} b_2 \\ a_2 \end{bmatrix} \tag{11}$$

or $v_1 = Tv_2$, where v_1 and v_2 are vectors containing the forward and backward wave amplitudes at the input and output of the set of five cells. The eigenvalues of T are $e^{-j\phi}$ and $e^{j\phi}$ where ϕ is the phase difference between output and input of the group of cells embedded in an infinite cascade of such networks. The calculation of ϕ should be done over a wide band including low frequencies and "unwrapped" to avoid jumps of 2π. The free space phase difference ϕ_0 can be calculated by (12), where λ is the free space wavelength, n_c is the number of cells considered, and C is the unit cell length.

$$\phi_0 = \frac{2\pi}{\lambda} n_c C \tag{12}$$

The velocity factor in the direction of the array of cells (y-axis), which is also the direction of propagation is:

$$v_y = \frac{\phi_0}{\phi} \tag{13}$$

The corresponding refractive index is of course $n_y = 1/v_y$. The velocity factors obtained are shown in Fig. 4 for both spherical and cubic inclusions. The plot shows that the velocity factors start to spread as a function of frequency as the sizes of the inclusions become larger and approach their resonant frequencies. The quantity 's' in the plot refers to the diameter

This article has been accepted for publication in a future issue of this journal, but has not been fully edited. Content may change prior to final publication. Citation information: DOI 10.1109/TAP.2020.3044638, IEEE Transactions on Antennas and Propagation

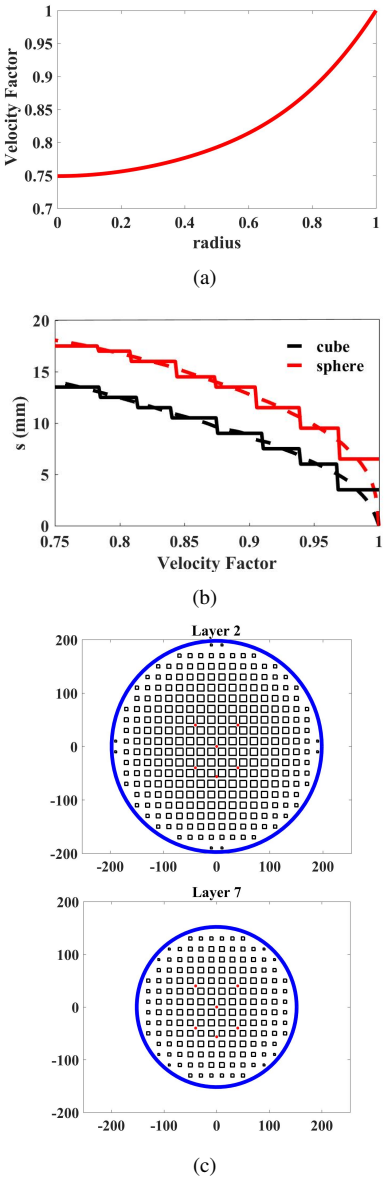

Fig. 5. Principal design steps. (a) Velocity factor as function of radius. (b) Size of inclusion as function of velocity factor (dashed) and quantized (solid) for cubic and spherical inclusions. (c) Allocate size of each inclusion based on ***r***, its distance from the center of the lens. Two layers shown.

in the case of spherical inclusions and the side length in the case of cubic inclusions.

The bandwidth of a Luneburg lens with a natural dielectric is in principle infinite. However, with an artificial dielectric the bandwidth is limited at high frequencies by the spread in the velocity factor that occurs as the conducting inclusions approach resonance. At lower frequencies the spread in velocity factor is much less and there is no low frequency limit.This has been addressed in the following sections.

The desired refractive index distribution for positioning the feed at $0.15R$ distance at the rear of the Luneburg lens is plotted in Fig. 5(a) as velocity factors. Ideally, spherical inclusions are preferred because of their symmetry. However, as the required velocity factors are in the range 0.75 to 1, if spherical inclusions are used it is seen in Fig. 4 that diameters up to 18 mm are needed with a spacing between centers of 20 mm. It was considered that controlling the tolerances of the location of the spheres in this situation would be difficult, so cubic inclusions were chosen as their maximum size is 14 mm for the required range of velocities.

Finally, for convenience of manufacture instead of using cubes of any size, eight sizes were chosen to span the required range of velocities factors. The allowable sizes were initially chosen to have equal steps in velocity factor and then rounded to the nearest 0.5 mm for ease of manufacture. This has resulted in the quantization scheme indicated in Fig. 5(b). These choices seem not to be critical. Full-wave analysis of radiation patterns has shown that any increase in the number of inclusion sizes or variation of the rounding of sizes made negligible difference to the patterns. If the aim were to minimize reflection, probably choosing the sizes to give equal steps in velocity factor ratio (equal steps in logarithm of velocity factor) would be appropriate.

Having chosen the quantization scheme, the size of each inclusion is found based on its radial distance from the center of the lens. The ideal velocity factor at that point is calculated from the data in Fig. 5(b) and the inclusion size from the set of permitted sizes with velocity factor nearest the desired one is chosen. This allows a size to be allocated to each of the cubic inclusions of the lens. Fig. 5(c) shows the resulting 2D layouts of two of the 20 layers of the lens. The black squares represent the inclusion positions and sizes.

C. Analysis of Anisotropy at Oblique Incidence and Compensation

In the case where the direction of propagation is inclined at an angle α to the y-direction, (13) still applies. However, in this case v_y is no longer the quantity of interest. Instead the velocity in the direction of propagation, v_k is required. This is given by (14).

$$v_k = v_y \cos\alpha \tag{14}$$

Another complication arises in the use of HFSS to arrive at values of v_y and v_k at an inclined angle. This is because the angle of propagation α_0 set in HFSS refers to the direction of propagation in free space whereas α is the direction of propagation in the artificial dielectric. When the incident wave enters the artificial dielectric at an inclined angle to the boundary, it undergoes a change in direction according to Snell's law:

$$\frac{\sin\alpha}{\sin\alpha_0} = v_k \tag{15}$$

Applying (14):

$$\tan\alpha = v_y \sin\alpha_0 \tag{16}$$

Since v_y is obtained from the HFSS analysis, (16) relates α_0 and α. However, since $\sin\alpha_0$ must be less than 1, the range of α is limited as:

$$\alpha < \tan^{-1} v_y \tag{17}$$

This article has been accepted for publication in a future issue of this journal, but has not been fully edited. Content may change prior to final publication. Citation information: DOI 10.1109/TAP.2020.3044638, IEEE Transactions on Antennas and Propagation

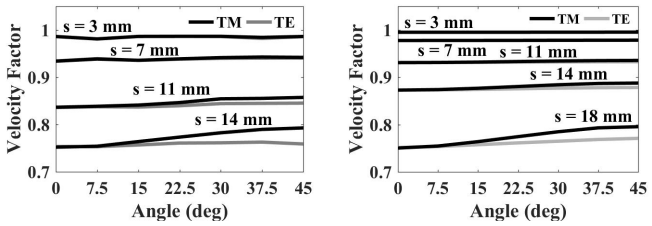

Fig. 6. Velocity factors as function of angle of incidence (α) for different size of inclusions at 3.5 GHz. (a) Cubic. (b) Spherical.

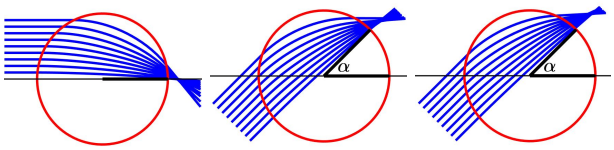

Fig. 7. Focusing characteristics for different azimuth angles showing movement of focus. (a) TE at 0° azimuth. (b) TE at 45°. (c) TM at 45°. In each case the rays converge to an accurate focus.

TABLE II
VARIATION OF POSITION OF FOCUS WITH AZIMUTH ANGLE

Azimuth angle (deg)	Distance of focus from lens surface (mm) TE	Distance of focus from lens surface (mm) TM
0	28.8 ± 3	28.8 ± 3
22.5	36.2 ± 7	50.7 ± 7
45	32.0 ± 10	74.8 ± 6

For the maximum inclusion size in this lens design, the range of propagation angle is restricted to $\alpha < 45°$. The variation in velocity factor as calculated using this method is shown in Fig. 6 for a range of sizes of cubic and spherical inclusions. The angle shown is α, the propagation angle within the artificial dielectric relative to the alignment of the inclusions. The plot shows that for small inclusions there is almost no variation in velocity factor with propagation angle. For larger inclusions, the propagation velocity rises (refractive index decreases) as the inclination angle increases. For large inclusions splitting occurs between TE and TM modes corresponding to vertical polarization (VP) and horizontal polarization (HP). These variations obviously affect the effective refractive index profile of the lens at different azimuth angles.

The focusing properties at boresight were examined by using the refractive index profile along the central ray path through the lens without taking account of the variation in refractive index resulting from the different angles of incidence of more oblique rays relative to the grid of the inclusions. Similarly, at other feed angles, the focusing characteristics can be analyzed approximately using the refractive index profile corresponding to the central ray. Based on the inclusion size versus radius plots in Fig. 5(a-b) that characterize the lens design, the velocity factor versus radius relationship that applies at a particular azimuth angle is obtained by interpolation of the data used to prepare Fig. 6.

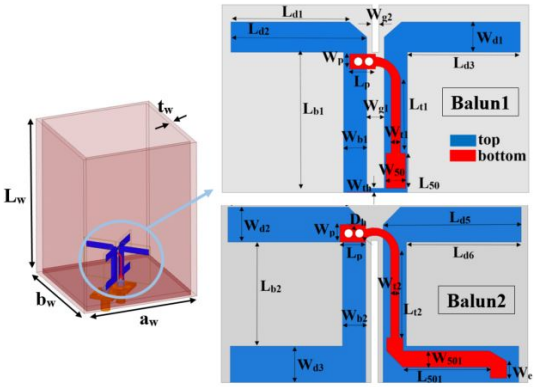

Fig. 8. Geometry of the square waveguide feed and detailed view of the PCB crossed dipoles oriented at 45° to the waveguide walls. SMA connectors are visible below the brass end short.

TABLE III
DIMENSIONS OF THE FEED.(UNIT:MM)

a_w	60	b_w	60	t_w	2.5	L_w	85
W_{d1}	3.3	W_{g1}	2	W_{b1}	2.7	W_{th}	0.5
W_{t1}	1.1	W_{g2}	0.8	W_p	1.75	L_p	3
L_{d1}	14.9	L_{d2}	16.9	L_{d3}	14.2	L_{b1}	15.7
L_{d4}	13.75	L_{d5}	15.97	L_{d6}	13.27	L_{b2}	12
L_{50}	4	L_{501}	10.11	L_{t1}	8.7	L_{t2}	10
W_{d2}	4	W_{d3}	4.2	W_{b2}	2.7	W_{t2}	1
W_{501}	1.89	W_{50}	2.3	W_e	2	D_h	1

Ray tracing is then carried out for different azimuth angles as was done for zero azimuth. The plots are shown in Fig. 7. The principal effect of the change of refractive index profile with azimuth angle is to move the focus further from the lens in the TM (i.e. HP) case. The plots show that while the focus moves with azimuth angle the rays still converge to an accurate focus. This opens the possibility of using a dielectric lens that preferentially focuses HP in front of the feed aperture to make the foci coincident. The variation of position of the foci with azimuth angle is summarized in Table II. The tolerances given refer to the standard deviation of the ray intersections with the optical axis. These provide an indication of the quality of the focus.

III. CONSTRUCTION AND DETAILED ANALYSIS OF LENS PERFORMANCE

A. Dual-Polarized Feed

A $\pm 45°$-polarized square waveguide feed was designed to excite the lens at different locations along the circumference of the lens. The waveguide is excited using a crossed dipole to produce dual-linearly polarized radiation. The configuration of the feed is shown in Fig. 8 and all dimensions are listed in Table III. The two red microstrip tracks from the dipoles come to 50 ohm lines and then connect to SMA connectors.

Two Arlon CuClad 250GT printed circuit boards (PCB) with a thickness of 0.75 mm and a dielectric constant of 2.6 are employed for the cross dipoles of the feed. An aluminum square section tube is used as the waveguide with a machined brass end short. The waveguide length is 85 mm (λ at 3.5 GHz) to suppress higher order modes in the aperture.

This article has been accepted for publication in a future issue of this journal, but has not been fully edited. Content may change prior to final publication. Citation information: DOI 10.1109/TAP.2020.3044638, IEEE Transactions on Antennas and Propagation

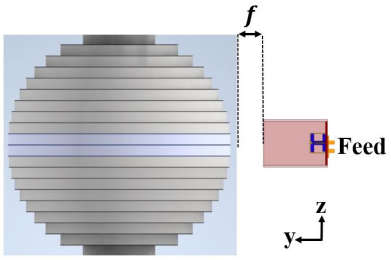

Fig. 9. 2D layout of the lens with feed showing spacing between feed aperture and lens surface.

B. Lens Performance with Multiple Feeds

The square waveguide feed is used to examine the lens's radiation performance. Fig. 9 shows the geometry of the lens with a feed in the yoz-plane. To examine the lens's performance as a function of pointing angle the feed is located at different angles around the lens, but always directed to the center of the lens.

As discussed in section II-B, at pointing angles approaching $45°$, the lens focal length increases. This is compensated for by increasing the radial offset of the feed from the lens surface. The value of the offset for a particular angle has been found by two methods. The first was by ray tracing using the refractive index variation due to angle of incidence, α relative to the inclusion grid and also by a full-wave analysis of the lens and feed. In the full-wave method the offset of the feed from the lens is varied and level of sidelobes adjacent to the main beam is determined. The focus is considered to be at the offset that gives the lowest sidelobe level (SLL). When the feed is located at the wrong distance from the lens, defocusing causes a quadratic phase error across the lens aperture which gives rise to increased SLL. This provides a more sensitive indication of correct focusing than other parameters such as gain. Results of the two methods are compared in Fig. 10(a). The results show considerable agreement despite the very different methods of calculation. This is particularly so since the phase center of the feed is calculated to lie 10.3 mm behind its aperture. This figure was determined from the calculated far-field phase pattern of the feed.

The simulated azimuth and elevation patterns at $+45°$ polarization with optimized feed locations are shown in Fig. 10(b) for 13 azimuth angles (α) at 3.5 GHz . The lens is symmetric about three orthogonal planes, so only the scanning in the azimuth plane is investigated as the results for the elevation plane are similar. The results for $+45°$ and $-45°$ polarization are similar, so the results for Port2 excitation ($-45°$-polarized) are not shown. The plots show that the simulated lens antenna gain is 23 dBi at boresight. The scanning loss is less than 0.8 dB.

Fig. 10(c) compares the simulated SLL in azimuth and elevation patterns at $+45°$ polarization with and without optimizing the feed location. The graph shows that the optimum feed position results in 4.5 dB reduction in SLL. It is noted that 'non-optimized feed position' in Fig.10(c) refers to the optimized position for $0°$ azimuth.

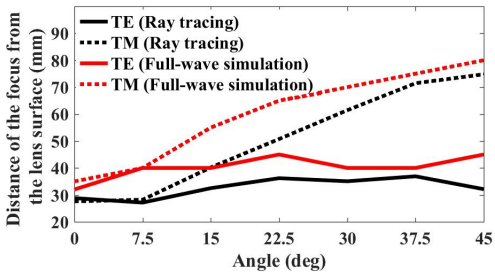

(a)

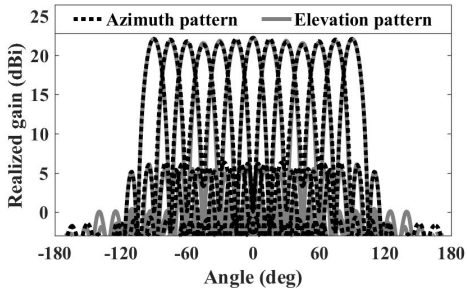

(b)

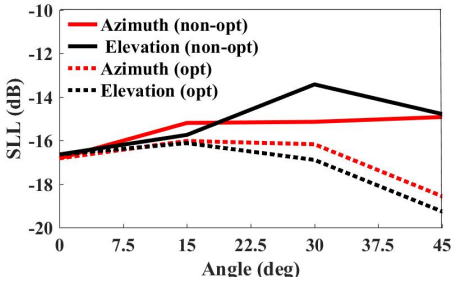

(c)

Fig. 10. Simulated performance of the lens antenna at 3.5 GHz. (a) Calculated distance of focus from lens surface by ray tracing and by full-wave simulation. (b) Realized gain of lens antenna with feed located at 13 azimuth/elevation positions spaced every $7°$ apart at optimum spacings based on sidelobes as shown in (a). (c) Improvement in SLL obtained by optimizing the distance between lens surface and feed aperture compared with a constant feed spacing which is optimum for $0°$ azimuth.

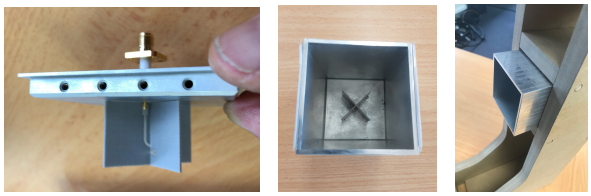

(a) (b) (c)

Fig. 11. Photographs of the feed (a) Back wall showing PCB crossed dipoles. (b) View into mouth of waveguide of assembled feed. (c) Feed located in test fixture.

IV. Fabrication and Results

A. Fabrication

Photographs of the feed are shown in Fig. 11 and of the lens with feed in Fig. 12. The lens is constructed from 20 circular layers of XPS foam of thickness 20 mm, which is the center to center spacing of the conducting inclusions. The density of foam used was 30 kg/m^3. Square holes were machined

This article has been accepted for publication in a future issue of this journal, but has not been fully edited. Content may change prior to final publication. Citation information: DOI 10.1109/TAP.2020.3044638, IEEE Transactions on Antennas and Propagation

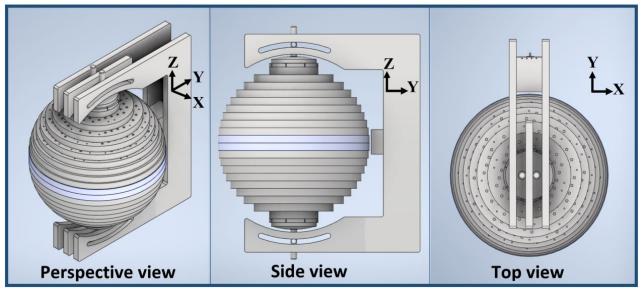

(a)

(b)

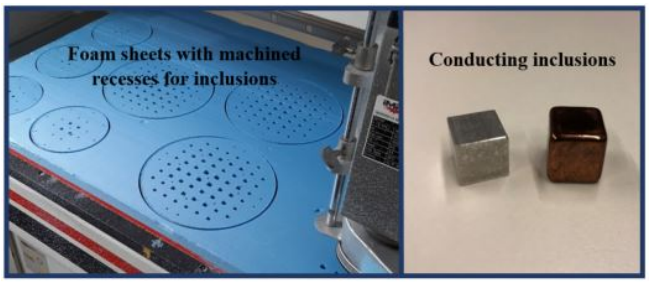

(c)

Fig. 12. Lens antenna fabrication and measurement. (a) Three views of lens mounted in test fixture. (b) Test fixture and lens mounted on positioner of far-field test range. The feed is visible in the r.h. photo. (c) Internal geometry of the fabricated lens prototype.

from one side of each foam sheet each of size 0.5 mm more than the size of the cubic inclusions. Each of these holes was machined to a depth so that when the inclusion was bedded down it was located midway between the two surfaces of the sheet. To allow the sheets to be assembled together with accurate orientation, alignment holes of 3 mm diameter were drilled at an appropriate radius in areas between the inserts. These are visible in Fig.5(c). Nylon rods passing through the alignment holes were used to align successive layers correctly. The machining of the foam layers was accomplished on NC equipment used for the manufacture of foam signage.

A total of 3840 conducting inclusions are required for this design. Two sets of conducting inclusions were made, one set of solid aluminum and one of copper plated Acrylonitrite Butodiene Styrene (ABS) plastic. The thickness of the copper coating is such that the electrical properties of the ABS have no effect. Each inclusion was inserted manually after applying a drop of superglue to its base. Obviously pick-and-place technology would be used in production. Pieces of thin double-sided adhesive tape were used to join adjacent layers. The 3 mm nylon rods were used to attach the assembled lens to plastic disks at the top and bottom of the lens for mounting purposes. The presence of these nylon rods had no discernible effect on the electrical performance of the lens. In Table IV the weight of the lens as implemented is compared with those of the same diameter using alternative technologies. The spherical Luneburg lens mounted in a test fixture and far-field measurement setup are shown in Fig. 12.

TABLE IV
COMPARISON OF THE WEIGHT OF THIS TYPE OF LENS OF THE SAME DIAMETER WITH DIFFERENT CONSTRUCTION METHODS

Lens construction	Mass of Lens (kg)
Solid dielectric (e.g. PTFE)	73.7
XPS foam with solid Aluminum inclusions	10.5
XPS foam with metal plated ABS inclusions	4.7

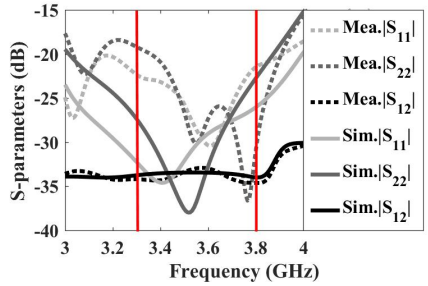

(a)

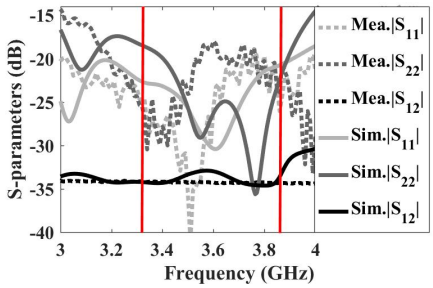

(b)

Fig. 13. Simulated (solid lines) and measured (dashed lines) return loss and isolation of (a) Feed (b) Lens and feed. Design bandwidth is indicated by vertical lines.

B. Reflection and Isolation Coefficients

An Agilent Network Analyzer N5225A was used for S-parameter measurements. The S-parameters of the square waveguide feed and lens antenna are shown in Fig. 13. The simulated and measured results are within expected agreement. The results demonstrate that from 3.3 to 3.8 GHz, the reflection coefficient of the lens and feed is less than -18 dB. The measured two port isolation is greater than 34 dB across the band.

This article has been accepted for publication in a future issue of this journal, but has not been fully edited. Content may change prior to final publication. Citation information: DOI 10.1109/TAP.2020.3044638, IEEE Transactions on Antennas and Propagation

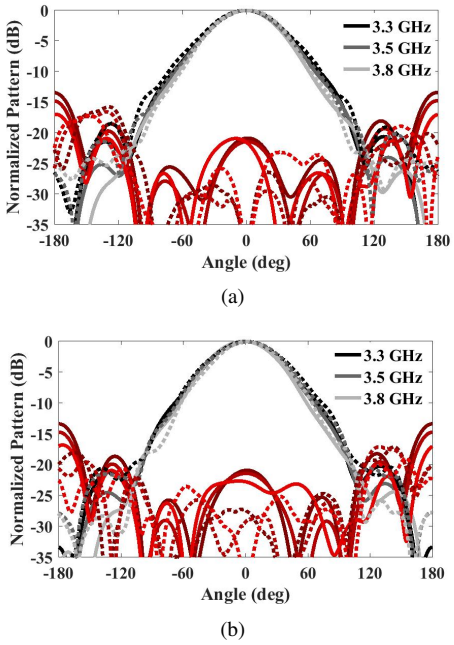

Fig. 14. Simulated (solid lines) and measured (dashed lines) co-polar (black lines) and cross-polar (red lines) azimuth radiation patterns of feed antenna, frequencies superimposed (a) Port1. (b) Port2.

C. Radiation Pattern, Gain, and Efficiency

The simulated and measured radiation patterns of the feed across the band between 3.3 and 3.8 GHz are shown in Fig. 14. The gain is about 8 dBi, and cross-polar ratio is below -20 dB. The 3 dB beamwidth in the azimuth plane is about 70° at the center frequency (3.5 GHz). The measured results agree well with the simulated ones. Far-field measurements of the lens antennas were made on a 100m far-field test range. The gain of the antenna was obtained by substituting a standard gain horn for the antenna-under-test. The measured and simulated radiation patterns of the lens antenna at different frequencies across the band between 3.3 and 3.8 GHz are shown in Fig. 15 for 0° and 45° azimuth offset of the lens. Comparison of the 0° and 45° azimuth patterns shows that at wider scan angles the SLL reduces from -15 dB to -20 dB, while the XPD degrades. This is attributed to the phase shift that the anisotropy of the lens introduces between VP and HP discussed in section II-C which causes the diagonal polarization to become elliptical.

In the prototype lens antenna, the offsets of the feed as a function of azimuth were selected to be midway between the calculated values for TE (VP) and TM (HP). However, it is worth mentioning that introducing a dielectric septum or metal stubs into the feed waveguide to delay the vertically polarized component relative to the horizontal component should almost eliminate the effect of anisotropy on the cross-polar ratio. These can be different for different azimuth angles. The normal specification on cross-polar applied to cellular base station antennas to minimize loss of diversity gain is that, over the 10 dB beamwidth, the cross-polar ratio should be below -8 dB. This requirement is met by this lens antenna without any change.

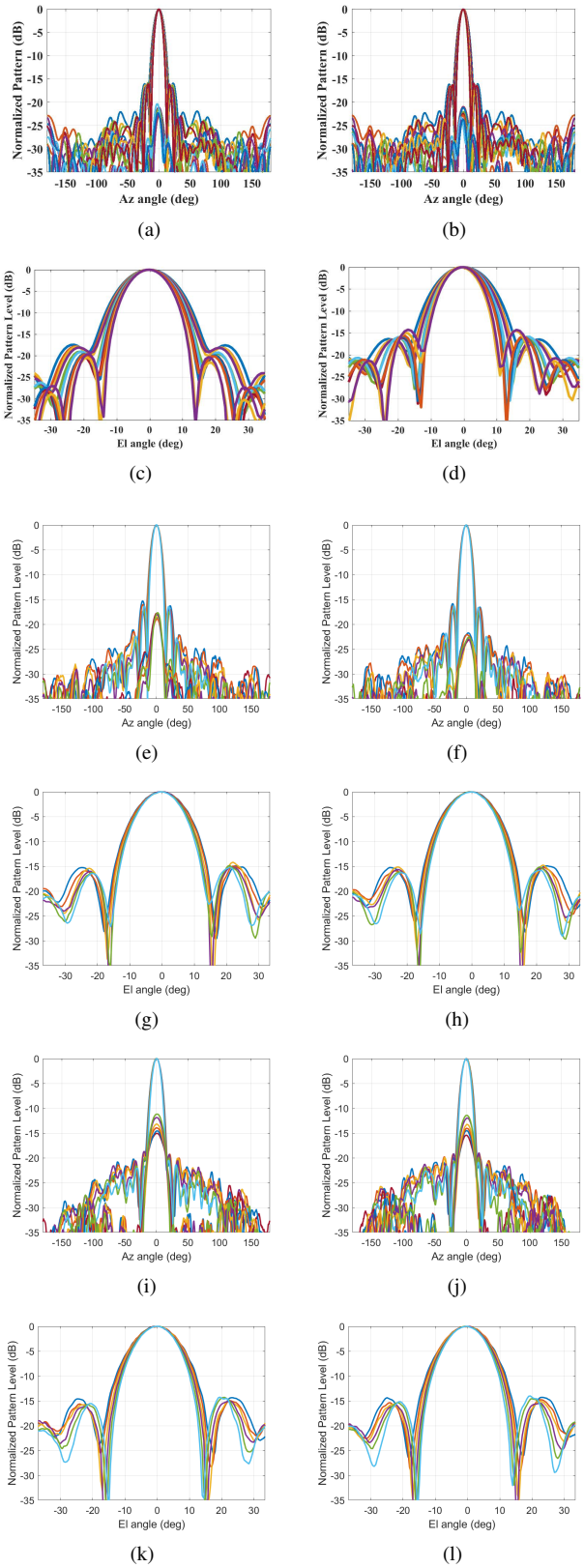

Fig. 15. Simulated and measured normalized patterns of lens antenna. Patterns superimposed for frequencies 3.3, 3.4, ...3.8 GHz. Cross-polar azimuth patterns superimposed. Feed at 0° azimuth. (a) Simulated azimuth pattern, Port 1. (b) Simulated azimuth pattern, Port 2. (c) Simulated elevation pattern, Port 1. (d) Simulated elevation pattern, Port 2. (e) Measured azimuth pattern, Port 1. (f) Measured azimuth pattern, Port 2. (g) Measured elevation pattern, Port 1. (h) Measured elevation pattern, Port 2. Feed at 45° azimuth. (i) Measured azimuth pattern, Port 1. (j) Measured azimuth pattern, Port 2. (k) Measured elevation pattern, Port 1. (l) Measured elevation pattern, Port 2.

This article has been accepted for publication in a future issue of this journal, but has not been fully edited. Content may change prior to final publication. Citation information: DOI 10.1109/TAP.2020.3044638, IEEE Transactions on Antennas and Propagation

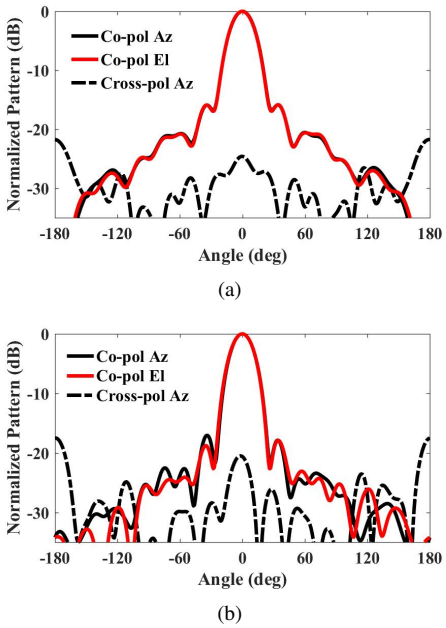

Fig. 16. Simulated normalized radiation patterns of lens antenna at 1.7 GHz. (a) Feed at 0° azimuth. (a) Feed at +45° azimuth.

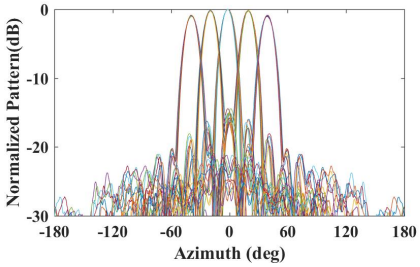

Fig. 17. Measured normalized patterns with feeds spaced 20° apart in azimuth. Patterns superimposed for frequencies 3.3, 3.4,...,3.8 GHz. (The patterns intersect at approximately -8 dB which is required in multicell applications.)

It is also noted that with MIMO processing, the effect of the phase shift between vertical and horizontal polarization (and hence of the measured cross-polar) will be removed.

In the lens antenna described here, a low frequency limit occurs because of low-frequency cut-off of the waveguide. To demonstrate the wideband performance of the lens (as distinct from the waveguide feed), the simulated radiation patterns of the same lens with a feed scaled to 1.7GHz are shown in Fig. 16. In comparison to the radiation patterns of the lens antenna at upper frequencies given in Fig. 15, the simulated results of the lens antenna at 1.7 GHz are broader, but still good. The results confirm the wideband performance of the lens between 1.7 GHz and 3.8 GHz with a gain difference of about 6 dB due to frequency and sidelobe level below -16 dB across the octave bandwidth.

To demonstrate the dual-polarized performance of multiple adjacent beams, the lens was measured with five feeds side by side in the optimized positions to produce a beam crossover level of -8 dB as required in multicell application. The measured radiation patterns of Port1 (+45°-polarized) of the lens antenna in the azimuth plane at different frequencies from 3.3 to 3.8 GHz are shown in Fig. 17. Five radiating beams are created which cover an angular range between ±50°. The measured gain versus frequency for dual slant polarization is shown in Fig. 18. The plots show that the gain difference between 0° and 45° azimuth is less than 0.8 dB across the band. Much of this difference is attributable to power lost in

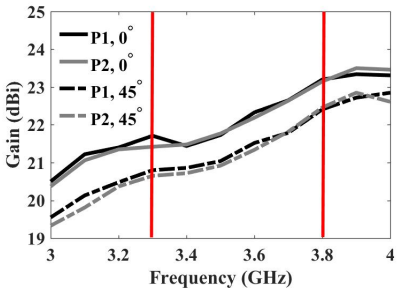

Fig. 18. Measured absolute gain for ports 1 and 2 at 0° azimuth and at 45°. Design bandwidth is indicated by vertical lines.

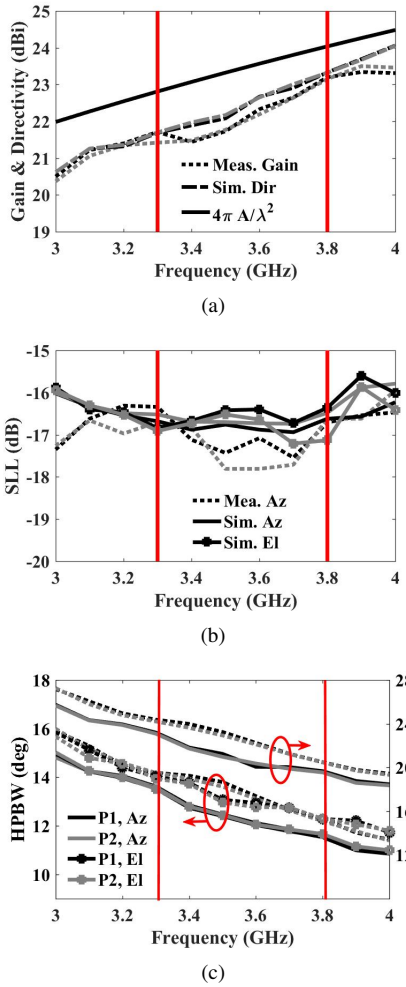

Fig. 19. Measured (dashed lines) and simulated (solid line) results of the Luneburg lens antenna for Port1 (black lines) and Port2 (grey lines) versus frequency at 0° azimuth . (a) Comparison of measured gain, simulated directivity, and $10\log(4\pi A/\lambda^2)$ (b) SLL in azimuth and elevation plane at 0 deg azimuth. (c) Azimuth and elevation 3 dB and azimuth 10 dB beamwidth.

TABLE V
COMPARISON OF THIS WORK WITH OTHER REPORTED LUNEBURG LENS ANTENNAS

Ref	Realization	Feed Type	Freq. Band (GHz)	RL (dB)	Scan Angle (deg)	Gain (dB)	HPBW (deg)	SLL (dB)	Aperture Efficiency (%)	Radiation Efficiency (%)	Crossover level (dB)	XPD at boresight (dB)	Pol.
[24]	Perforated slices	Open-ended waveguide	26.5-40	>12	n.g.	22-28	3.5/4.6	-15/-20	22-50	n.g.	n.g.	-15	LP
[25]	Perforated slices	Open-ended waveguide	12-18	>14	±75	23.1-25.7	11/14	-9/-22.8	47-93	80	n.g.	n.g.	LP
[30]	3D Printing (cubes)	Open-ended waveguide	8-12	>10	n.g.	17.3-20.3	13/19	-20/-25	47-53	n.g.	n.g.	n.g.	LP
[31]	3D Printing (cubes)	Open-ended waveguide	28-37	>10	n.g.	19-26	n.g.	-18/-9	n.g.	n.g.	n.g.	n.g.	LP
[23]	3D Printing (rings)	ME-dipole	26-40	>10	±61	18.6-21.2	12.8/12.4	-16/-15	46-54	75	-2.6 to -5	-35	LP
[21]	3D Printing (Icosahedron)	Ridged-waveguide	26.5-37	>10	±44	19-21.2	n.g.	-15/-18	46-85	70	-8 to -10	n.g.	CP
This	Conductive cubes	Open-ended waveguide	3.3-3.8	>18	±60	21.9-23.4	13/14.5	-16/-16	75-85	91	-8	-18	Dual-LP

⋆ **HPBW: half-power beamwidth; n.g.:not given; RL: return loss; SLL: sidelobe level; XPD: cross polarization discrimination**.

the cross-polar pattern. In the measured patterns, no sign of effects due to blockage by neighboring feeds is visible.

The diagrams in Fig. 19(a) compare the measured gain and the simulated directivity with maximum ideal directivity ($10\log(4\pi A/\lambda^2)$, A is the cross section area of the lens) across the band. The realized gain varies from 21.5 to 23 dBi within the band 3.3 to 3.8 GHz. The variation of the gain is less than 1.5 dB, 1.2 dB of which is expected from the bandwidth. The measured gain is less than 0.3 dB lower than the simulated directivity. The estimated root mean squared error (RMSE) of the gain measurements is 0.35 dB. It is seen that foam and metal conductors can provide extremely low loss. Comparable panel antennas would generally have losses exceeding 2 dB. The difference between the ideal directivity based on the cross section area of the lens and the measured gain is only 1 dB. This includes losses due to the taper and power from the feed that does not reach the lens. Fig. 19(b) compares the simulated and measured SLL in the azimuth plane and simulated SLL in the elevation plane, which are below -16 dB in both planes. Fig. 19(c) shows the measured E-plane and H-plane -3 dB beam width of the lens antenna is decreasing from 14.5° to 13° with the increase in frequency. The azimuth -10 dB beamwidth is shown as this indicates the cellular coverage of each beam.

D. Comparison and Discussion

The characteristics of this lens antenna are compared to other Luneburg lens antennas reported in the literature and the results are listed in Table V. In most reported designs, a wide bandwidth open-ended waveguide is employed as the feed, but generally only for single polarization [23]–[25], [30], [31]. Although feeds of this type have their phase center inside the waveguide, it is not clear whether the spacing of the feed from the lens surface was optimized for minimum sidelobe level. The bandwidth listed in Table V for this work refers to the lens antenna with feed waveguide, which is narrow band. However, the lens itself has a bandwidth exceeding an octave. This exceeds the fractional bandwidths of the other listed works. Multibeam radiation using dipole fed by substrate integrated waveguide (SIW) are described in [23] with 3D printed dielectric rings. This type of construction is unsuitable for use at frequencies below around 10 GHz as the mass and volume of the dielectric becomes excessive. The lens antenna in this work provides superior efficiency with broad scanning range. This design realizes dual slant polarizations and allows -8 dB crossover level between the beams as required for most cellular applications.

V. CONCLUSION

A high-gain antenna has been presented using a novel 3D Luneburg lens fed by dual-linearly polarized feed. The lens is constructed using a light-weight and low cost method suitable for use at frequencies below 12 GHz. The artificial dielectric material is made of conducting inclusions embedded in low density foam which makes for very low loss. The use of equal spacings of the inclusions allows the lens to be made in planar layers which greatly simplifies the manufacture of the lens. However, this gives rise to some anisotropy in the lens's performance which can be largely overcome by varying the spacing of the feed from the lens surface. The concept has been proved by measurement of a prototype, in which simulated and experimental results agree well. The lens antenna presented here is suitable for high capacity event coverage, fixed wireless coverage, high gain multibeam for rural application, multibeam 4G and 5G. The design is a more economical alternative to massive MIMO, with some comparison of capacity. It is also a high-gain high-capacity alternative to existing base station antennas.

ACKNOWLEDGMENT

The authors would like to thank Vecta Pty Ltd for testing the prototype antenna on their far-field antenna range. The authors would also like to thank Prof. Richard W. Ziolkowski, University of Technology Sydney, for valuable discussions.

REFERENCES

[1] R. K. Luneburg, *Mathematical theory of optics*. Univ of California Press, 1964.

[2] H. Xin, J. B. West, J. C. Mather, J. Doane, J. A. Higgins, H. Kazemi, and M. J. Rosker, "A two-dimensional millimeter wave phase scanned lens utilizing analog electromagnetic crystal (emxt) waveguide phase shifters," *IEEE transactions on antennas and propagation*, vol. 53, no. 1, pp. 151–159, 2005.

[3] O. Quevedo-Teruel, M. Ebrahimpouri, and F. Ghasemifard, "Lens antennas for 5g communications systems," *IEEE Communications Magazine*, vol. 56, no. 7, pp. 36–41, 2018.

[4] Q. Liao, N. Fonseca, and O. Quevedo-Teruel, "Compact multibeam fully metallic geodesic luneburg lens antenna based on non-euclidean transformation optics," *IEEE Transactions on Antennas and Propagation*, vol. 66, no. 12, pp. 7383–7388, 2018.

[5] Y. Geng, J. Wang, Y. Li, Z. Li, M. Chen, and Z. Zhang, "Radiation pattern-reconfigurable leaky-wave antenna for fixed-frequency beam steering based on substrate-integrated waveguide," *IEEE Antennas and Wireless Propagation Letters*, vol. 18, no. 2, pp. 387–391, 2019.

[6] J.-W. Lian, Y.-L. Ban, Q.-L. Yang, B. Fu, Z.-F. Yu, and L.-K. Sun, "Planar millimeter-wave 2-d beam-scanning multibeam array antenna fed by compact siw beam-forming network," *IEEE Transactions on Antennas and Propagation*, vol. 66, no. 3, pp. 1299–1310, 2018.

[7] M. Ansari, H. Zhu, N. Shariati, and Y. J. Guo, "Compact planar beamforming array with endfire radiating elements for 5g applications," *IEEE Transactions on Antennas and Propagation*, vol. 67, no. 11, pp. 6859–6869, 2019.

[8] J.-W. Lian, H. Zhu, Y.-L. Ban, D. K. Karmokar, and Y. J. Guo, "Uniplanar high-gain 2-d scanning leaky-wave multibeam array antenna at fixed frequency," *IEEE Transactions on Antennas and Propagation*, 2020.

[9] J.-W. Lian, Y.-L. Ban, H. Zhu, and Y. Guo, "Reduced-sidelobe multibeam array antenna based on siw rotman lens," *IEEE Antennas and Wireless Propagation Letters*, 2019.

[10] Y. J. Guo and B. Jones, *Base Station Antennas, in John Volakis ed., Chapter 40, Antenna Engineering Handbook*. McGraw-Hill, 2018.

[11] J. Thornton and K.-C. Huang, *Modern lens antennas for communications engineering*. John Wiley & Sons, 2013, vol. 39.

[12] X. Gao, L. Dai, S. Han, I. Chih-Lin, and X. Wang, "Reliable beamspace channel estimation for millimeter-wave massive mimo systems with lens antenna array," *IEEE Transactions on Wireless Communications*, vol. 16, no. 9, pp. 6010–6021, 2017.

[13] H.-T. Chou and Z.-D. Yan, "Parallel-plate luneburg lens antenna for broadband multibeam radiation at millimeter-wave frequencies with design optimization," *IEEE Transactions on Antennas and Propagation*, vol. 66, no. 11, pp. 5794–5804, 2018.

[14] C. Hua, X. Wu, N. Yang, and W. Wu, "Air-filled parallel-plate cylindrical modified luneberg lens antenna for multiple-beam scanning at millimeter-wave frequencies," *IEEE transactions on microwave theory and techniques*, vol. 61, no. 1, pp. 436–443, 2012.

[15] A. B. Numan, J.-F. Frigon, and J.-J. Laurin, "Printed w-band multibeam antenna with luneburg lens-based beamforming network," *IEEE Transactions on Antennas and Propagation*, vol. 66, no. 10, pp. 5614–5619, 2018.

[16] C. Wang, J. Wu, and Y.-X. Guo, "A 3-d-printed wideband circularly polarized parallel-plate luneburg lens antenna," *IEEE Transactions on Antennas and Propagation*, vol. 68, no. 6, pp. 4944–4949, 2019.

[17] P. Liu, X.-W. Zhu, Y. Zhang, Z. H. Jiang, X. Wang, W. Hong, and T. H. LE, "A novel e-plane-focused cylindrical luneburg lens loaded with metal grids for side lobe level reduction," *IEEE Transactions on Antennas and Propagation*, 2019.

[18] C. Mateo-Segura, A. Dyke, H. Dyke, S. Haq, and Y. Hao, "Flat luneburg lens via transformation optics for directive antenna applications," *IEEE Transactions on Antennas and Propagation*, vol. 62, no. 4, pp. 1945–1953, 2014.

[19] Y. Su and Z. N. Chen, "A radial transformation-optics mapping for flat ultra-wide-angle dual-polarized stacked grin mtm luneburg lens antenna," *IEEE Transactions on Antennas and Propagation*, vol. 67, no. 5, pp. 2961–2970, 2019.

[20] Z. Larimore, S. Jensen, A. Good, A. Lu, J. Suarez, and M. Mirotznik, "Additive manufacturing of luneburg lens antennas using space-filling curves and fused filament fabrication," *IEEE Transactions on Antennas and Propagation*, vol. 66, no. 6, pp. 2818–2827, 2018.

[21] C. Wang, J. Wu, and Y.-X. Guo, "A 3d-printed multibeam dual circularly polarized luneburg lens antenna based on quasi-icosahedron models for ka-band wireless applications," *IEEE Transactions on Antennas and Propagation*, 2020.

[22] R. Ryazantsev, Y. Salomatov, V. Panko, and M. Sugak, "Flat-layered spherical lens antenna system in conditions of slant polarized feeder radiation," in *2016 International Siberian Conference on Control and Communications (SIBCON)*. IEEE, 2016, pp. 1–3.

[23] Y. Li, L. Ge, M. Chen, Z. Zhang, Z. Li, and J. Wang, "Multibeam 3-d-printed luneburg lens fed by magnetoelectric dipole antennas for millimeter-wave mimo applications," *IEEE Transactions on Antennas and Propagation*, vol. 67, no. 5, pp. 2923–2933, 2019.

[24] S. Rondineau, M. Himdi, and J. Sorieux, "A sliced spherical luneburg lens," *IEEE Antennas and Wireless Propagation Letters*, vol. 2, pp. 163–166, 2003.

[25] H. F. Ma, B. G. Cai, T. X. Zhang, Y. Yang, W. X. Jiang, and T. J. Cui, "Three-dimensional gradient-index materials and their applications in microwave lens antennas," *IEEE Transactions on Antennas and Propagation*, vol. 61, no. 5, pp. 2561–2569, 2013.

[26] H. F. Ma and T. J. Cui, "Three-dimensional broadband and broad-angle transformation-optics lens," *Nature communications*, vol. 1, no. 1, pp. 1–7, 2010.

[27] S. Matitsine, "Artificial dielectric material and method of manufacturing the same," Aug. 27 2013, uS Patent 8,518,537.

[28] C. L. Holloway, E. F. Kuester, J. Baker-Jarvis, and P. Kabos, "A double negative (dng) composite medium composed of magnetodielectric spherical particles embedded in a matrix," *IEEE Transactions on Antennas and Propagation*, vol. 51, no. 10, pp. 2596–2603, 2003.

[29] R. W. Ziolkowski, "Design, fabrication, and testing of double negative metamaterials," *IEEE Transactions on antennas and Propagation*, vol. 51, no. 7, pp. 1516–1529, 2003.

[30] M. Liang, W.-R. Ng, K. Chang, K. Gbele, M. E. Gehm, and H. Xin, "A 3-d luneburg lens antenna fabricated by polymer jetting rapid prototyping," *IEEE Transactions on Antennas and Propagation*, vol. 62, no. 4, pp. 1799–1807, 2014.

[31] K. F. Brakora, J. Halloran, and K. Sarabandi, "Design of 3-d monolithic mmw antennas using ceramic stereolithography," *IEEE transactions on antennas and propagation*, vol. 55, no. 3, pp. 790–797, 2007.